Research papers

Sensitivity of growth characteristics of tidal sand ridges and long bed waves to formulations of bed shear stress, sand transport and tidal forcing: A numerical model study

Bing Yuan *, Huib E. de Swart, Carles Panadès

Institute for Marine and Atmospheric research Utrecht, Utrecht University, Princetonplein 5, 3584CC Utrecht, The Netherlands

ARTICLE INFO

ABSTRACT

Tidal sand ridges and long bed waves are large-scale bedforms that are observed on continental shelves. They differ in their wavelength and in their orientation with respect to the principal direction of tidal currents. Previous studies indicate that tidal sand ridges appear in areas where tidal currents are above 0.5 m s^{-1}, while long bed waves occur in regions where the maximum tidal current velocity is slightly above the critical velocity for sand erosion and the current is elliptical. An idealized nonlinear numerical model was developed to improve the understanding of the initial formation of these bedforms. The model governs the feedbacks between tidally forced depth-averaged currents and the sandy bed on the outer shelf. The effects of different formulations of bed shear stress and sand transport, tidal ellipticity and different tidal constituents on the characteristics of these bedforms (growth rate, wavelength, orientation of the preferred bedforms) during their initial formation were examined systematically.

The results show that the formulations for bed shear stress and slope-induced sand transport are not critical for the initial formation of these bedforms. For tidal sand ridges, under rectilinear tidal currents, increasing the critical bed shear stress for sand erosion decreases the growth rate and the wavelength of the preferred bedforms significantly, while the orientation angle slightly decreases. The dependence of the growth rate, wavelength and the orientation of the preferred bedforms on the tidal ellipticity is non-monotonic. A decrease in tidal frequency results in preferred bedforms with larger wavelength and smaller orientation angle, while their growth rate hardly changes. In the case of joint diurnal and semidiurnal tides, or spring-neap tides, the characteristics of the bedforms are determined by the dominant tidal constituent. For long bed waves, the number of anticyclonically/cyclonically oriented bedforms with respect to the principal current direction increases as the ellipticity of the cyclonic/anticyclonic tidal currents increases. Besides, under anticyclonic tidal currents, the growth rate of cyclonically oriented long bed waves increases as the tidal ellipticity increases. The model was also used to provide a possible explanation for the fact that the Dutch Banks have a larger wavelength than that of the Flemish Banks in the North Sea.
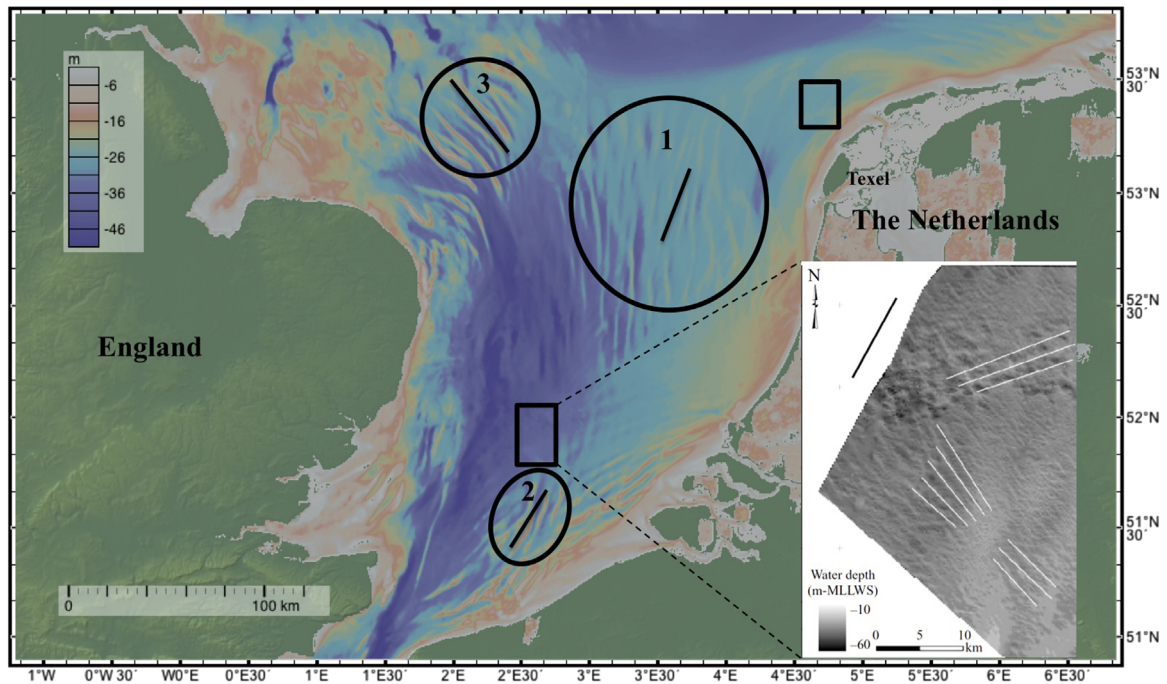
1. Introduction

Tidal sand ridges are observed on the continental shelves of many shallow seas with sandy beds where the tidal current is larger than about 0.5 m s^{-1} (Off, 1963; Liu et al., 1998; Dyer and Huntley, 1999 and references therein). Examples are the shelves of the North Sea (Fig. 1) and the East China Sea. These rhythmic seabed features have a typical wavelength (the distance from crest to crest) of order 10 km and a height of order 10 m. Their crests are oriented slightly cyclonically (5° to 30°) with respect to the principal direction of the tidal current, and they evolve on a time scale of centuries. Until recently, it was stated that other offshore rhythmic bottom patterns had considerably smaller length scales than those of tidal sand ridges (sand waves: wavelength of about 500 m; megaripples: wavelength of about 10 m), and that the crests of these smaller scale bedforms were orthogonal to the direction of the principal current (McCave, 1979). This perspective changed when Knaapen et al. (2001) identified a new type of large-scale bedforms on the outer shelf of the southern North Sea (Fig. 1). These so-called long bed waves have wavelengths in the range of 1–3 km. Later, van Dijk et al. (2011) reported the presence of another patch of long bed waves north of Texel and Vlieland on the Dutch continental shelf. Besides their smaller spacings, long

* Corresponding author.
E-mail addresses: b.yuan@uu.nl (B. Yuan), H.E.deSwart@uu.nl (H.E. de Swart), C.PanadesGuinart@uu.nl (C. Panadès).

http://dx.doi.org/10.1016/j.csr.2016.08.002
0278-4343/© 2016 Elsevier Ltd. All rights reserved.

Fig. 1. Bathymetry of the southern North Sea. The black circles indicate the areas where tidal sand ridges are located: (1) the Dutch Banks, (2) the Flemish Banks, and (3) the Norfolk Banks. Black lines inside the circles qualitatively indicate the principal direction of tidal currents based on Davies and Furnes (1980). The rectangular boxes show the areas where long bed waves are observed. In the map on the bottom right, the crests of long bed waves are marked by white lines, and the black line indicates the principal current direction (from TNO, on courtesy of T. van Dijk). The main map is obtained using GeoMapApp (Ryan et al., 2009).

bed waves differ from tidal sand ridges in their orientation, i.e., their crests are around 60° cyclonically or 30° anticyclonically rotated with respect to the principal current direction, as is shown in the bottom map of Fig. 1. The formation time scale of long bed waves, from the perspective of available field data, is unclear. The large-scale bedforms mentioned above provide not only habitats for marine organisms, but also potential resources of sand for beach nourishment. Knowledge of these seabed features and their dynamics is important for the stability of underwater structures and strategic planning of marine sand mining (van Lancker et al., 2010).

The formation of tidal sand ridges has been explained as a free instability of the system that describes the interaction between the sandy sea bed and the tidal currents (Huthnance, 1982; Hulscher et al., 1993). For this, linear stability analysis was conducted, with which the evolution of infinitesimal bottom perturbations on an otherwise flat bed, subject to tide-induced sand transport, was quantified. It turns out that linear stability analysis yields a wavelength and an orientation of the preferred bedform that are in fair agreement with those of many ridges observed in the field.

In the above cited studies and in later work on the initial formation of tidal sand ridges (Carbajal and Montaño, 2001; Roos et al., 2001; Walgreen et al., 2002), several simplifications in the bed shear stress, tidal forcing and the sand transport were used. First, a linearized bed shear stress was employed. The sensitivity of the growth characteristics of tidal sand ridges to the formulation of bed shear stress has not been systematically investigated yet. Second, the tidal forcing employed was simple, i.e., only one tidal constituent was used or only rectilinear tidal currents were considered. Roos et al. (2001) and Walgreen et al. (2002) imposed several, yet rectilinear, tidal constituents (residual current, semidiurnal lunar tide M_2 and quarter-diurnal tide M_4) to study the effect of tidal asymmetry on the characteristics of tidal sand ridges. In reality, tidal currents are elliptical rather than rectilinear. Moreover, they are composed of several other principal tidal constituents, such as the diurnal tide K_1 and the semidiurnal solar

tide S_2, which together with M_2 give rise to a mixed semidiurnal tide and a spring-neap tide, respectively. The effects of mixed tides and spring-neap tides on the formation of tidal sand ridges have not been studied yet. Third, the sand transport formulations used in these studies were highly simplified, i.e., both the threshold of sand erosion (Miller et al., 1977 and references therein) and anisotropic bottom slope-induced sand transport (Talmon et al., 1995) were neglected.

With regard to long bed waves, their initial formation has only been studied in Blondeaux et al. (2009), in which a depth-averaged hydrodynamic model was employed. Using linear stability analysis, they demonstrated that under the conditions that the tidal currents are elliptical and the maximum velocity is just above the threshold for sand erosion, long bed waves form alongside tidal sand ridges. In contrast, if the tides are rectilinear or the velocity is stronger, only tidal sand ridges are observed.

The considerations above motivate the two aims in this study. The first aim is to quantify the dependence of growth rate, wavelength and crest orientation of large-scale offshore tidal bottom patterns on formulations for (1) bed shear stress, (2) sand transport (critical shear stress on/off, an-/isotropic slope-induced transport), and (3) tidal forcing (ellipticity, diurnal/mixed tides, spring-neap tides). The second one is to gain more detailed insight into the formation of long bed waves, specifically, to assess the importance of nonlinear bed shear stress, critical bed shear stress, anisotropic sand transport, tidal ellipticity and current velocity on the formation of long bed waves.

To fulfill these aims, a numerical morphodynamic model was developed, which governs feedbacks between tidally forced depth-averaged currents and the sandy bed on an open domain that represents the outer shelf. There are several advantages to use a numerical model, as is done in the present study. First, unlike linear stability models which all employ the rigid-lid approximation, the time-dependent surface elevation is maintained in the present model. Second, linear stability models require explicit linearization of all equations and in particular for sand transport,

which is often a laborious and delicate task. In the present model, this is not needed. Third, comparison of output of the numerical model with that of linear stability models is useful to validate the numerical model. If successful, the latter can be subsequently employed to investigate the long-term nonlinear evolution of these large-scale bedforms. This approach was also adopted to study the initial formation of other coastal bedforms, such as sand bars on planar beaches (Deigaard et al., 1999; Klein and Schuttelaars, 2005) and tidal sand waves (Borsje et al., 2013). Note that in the latter study, model results were not compared with those of linear stability models.

The numerical model is a modification of that developed by Caballeria et al. (2002) and Garnier et al. (2006) to study the generation of rhythmic bottom patterns in the micro-tidal surf zone where wind waves play a key role. The main differences from the previous models concern the implementation of an open domain with no sloping bottom, periodic boundary conditions in both horizontal directions, tidal currents instead of wind- and wave-driven currents, and tidally-averaged sand transport.

The manuscript is organized as follows. In Section 2, the morphodynamic model is introduced, after which the linear stability analysis is explained briefly, followed by a description of the numerical implementation and the setup of the simulations. Results are presented in Section 3 and subsequently discussed in Section 4. Finally, Section 5 contains the conclusions.

2. Material and methods

2.1. Model

The morphodynamic model consists of modules for the currents, sand transport and the bed evolution. Following Hulscher et al. (1993), the currents are assumed to be governed by the depth-averaged shallow water equations, which read

$$\frac{\partial D}{\partial t} + \nabla \cdot (D\vec{u}) = 0, \tag{1}$$

$$\frac{\partial \vec{u}}{\partial t} + (\vec{u} \cdot \nabla)\vec{u} + f\vec{e}_z \times \vec{u} = -g\nabla\zeta - \frac{\vec{\tau_b}}{\rho D}. \tag{2}$$

Here, D is the local water depth, given by $D = \zeta + H - h$, with ζ the surface elevation, H the undisturbed water depth and h the bed level with respect to the reference bottom level (Fig. 2). Vector $\vec{u}$ is the depth-averaged flow velocity, whose components in the x- and y-directions are u and v, respectively, and $\vec{e}_z$ is a unit vector in the vertical direction. Note that in the cross product $\vec{e}_z \times \vec{u}$, vector $\vec{u}$ is interpreted as a three-dimensional vector, with a zero vertical
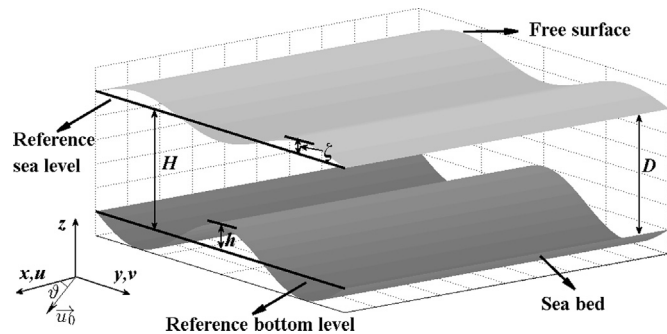

Fig. 2. Sketch of the model geometry, also showing the spatially uniform tidal current vector $\vec{u_0}$ in the principal direction, and its angle ϑ with respect to the x-axis.

component, and that only the horizontal components of the cross product are considered. Furthermore, t is time, $\nabla = (\partial/\partial x, \partial/\partial y)$ is the horizontal nabla operator, $f = 2\Omega\sin\Phi$ is the Coriolis parameter, with Ω the angular frequency of the Earth and Φ the latitude. Finally, g is the gravitational acceleration, ρ is the constant water density, and $\vec{\tau_b}$ is the bed shear stress vector, for which specific formulations are given in Subsection 2.2.

Since tidal sand ridges and long bed waves are observed on the outer shelf, this study focuses on the initial formation of bedforms due to tides in a flat and open area. Eqs. (1) and (2) are considered in a finite domain $0 \leq x \leq L_x$, $0 \leq y \leq L_y$, which represents a small part of the outer shelf far away from the coast. Typical values of L_x and L_y are 10–40 km, which are in the order of the wavelength of large-scale bedforms. On the outer shelf, the wavelength of the tidal waves L_t is approximately 400 km for a semidiurnal tide in water with a depth of the order of 10 m, hence it is assumed that L_x and L_y are much smaller than L_t. The assumption L_x, $L_y \ll L_t$ implies that, to a first approximation, the tidal wave is spatially uniform within the domain, which allows for imposing spatially uniform tidal forcing and periodic boundary conditions.

The water motion is forced by a time-varying horizontal pressure gradient force per unit mass $\vec{F_p}$. The force is associated with the presence of a large-scale tidal wave, and $\vec{F_p}$ drives a spatially uniform tidal current $\vec{u_0}$ that obeys

$$\frac{\partial \vec{u_0}}{\partial t} + f\vec{e}_z \times \vec{u_0} + \frac{\vec{\tau_{b_0}}}{\rho H} = \vec{F_p}, \quad \vec{F_p} = -g\nabla\zeta_0. \tag{3}$$

Clearly, since the bed shear stress $\vec{\tau_{b_0}}$ is determined by $\vec{u_0}$, $\vec{F_p}$ defines $\vec{u_0}$, or vice versa. The assumptions underlying Eq. (3) are twofold. First, the magnitude of free surface variations ζ_0 is much smaller than the mean water depth H. Second, the large-scale tidal wave is unaffected by topographic variations that act on scales L_x, $L_y \ll L_t$.

Setting $\zeta = \zeta_0 + \tilde{\zeta}$ and $D = \tilde{D} + \zeta_0$, where $\tilde{\zeta}$ stands for the surface elevation induced by the varying topography, and recalling that $|\zeta_0| \ll H$, the continuity equation and the momentum equation are rewritten as

$$\frac{\partial \tilde{D}}{\partial t} + \nabla \cdot (\tilde{D}\vec{u}) = 0, \tag{4}$$

$$\frac{\partial \vec{u}}{\partial t} + (\vec{u} \cdot \nabla)\vec{u} + f\vec{e}_z \times \vec{u} = -g\nabla\tilde{\zeta} + \vec{F_p} - \frac{\vec{\tau_b}}{\rho\tilde{D}}. \tag{5}$$

The components u_0 and v_0 of the spatially uniform tidal current $\vec{u_0}$ that results from the pressure gradient force $\vec{F_p}$ in the absence of bottom undulations are expressed as harmonic series:

$$u_0 = U_0 + \sum_i \left[a_i\cos(\omega_i t - \phi_i)\cos\vartheta_i - b_i\sin(\omega_i t - \phi_i)\sin\vartheta_i \right], \tag{6a}$$

$$v_0 = V_0 + \sum_i \left[a_i\cos(\omega_i t - \phi_i)\sin\vartheta_i + b_i\sin(\omega_i t - \phi_i)\cos\vartheta_i \right]. \tag{6b}$$

Here, U_0 and V_0 are the horizontal components of the residual flow (not considered in this study), the subscript i represents different tidal constituents, ω_i and ϕ_i are the angular frequency and phase of the tidal constituent, a_i and b_i are the semi-major and semi-minor axes of the tidal ellipse, and ϑ_i is the inclination of the long axis of the tidal ellipse with respect to the x-direction (Fig. 2). Consistent with earlier studies, the ellipticity of a tidal constituent is defined as the ratio between the semi-minor and semi-major axes of the tidal ellipse, i.e., $\varepsilon_i = b_i/a_i$. In the Northern Hemisphere,

positive ε_i means that the tidal current is cyclonic, while negative ε_i implies an anticyclonic current.

The bed level evolution is governed by the mass conservation of sediment,

$$(1-p)\frac{\partial h}{\partial t} + \nabla \cdot \vec{q} = 0. \tag{7}$$

Here, $\vec{q}$ is the volumetric sand transport per unit width (formulations are given in Section 2.2), and p is the bed porosity (typically ~0.4). The evolution of tidally induced bedforms is, to a good approximation, related to convergence of net sand transport that results from averaging over a tidal cycle. This is because the evolution time scales of those bedforms are much larger than the tidal period. The justification for the approximation follows from scaling arguments and the averaging theory that is discussed in Sanders et al. (2007). Hence, the bed level is assumed to be fixed when computing the hydrodynamics over a tidal cycle, and Eq. (7) is averaged over the tidal period, which results in

$$(1-p)\frac{\partial h}{\partial t} + \nabla \cdot \left\langle \vec{q} \right\rangle = 0. \tag{8}$$

Here, $\left\langle \cdot \right\rangle = T^{-1}\int_0^T \cdot \, dt$ stands for tidal average, where T is the tidal period. For currents with more than one tidal constituent, the tidal period is calculated as the least common multiple of the periods of the tidal constituents. In summary, the final system to be solved consists of Eqs. (4), (5) and (8), with $\vec{F}_p$ chosen such that in the absence of bottom undulations the flow is described by Eq. (6).

2.2. Formulations of bed shear stress and sand transport

To check the sensitivity of the initial formation of tidal sand ridges and long bed waves to using a linearized/nonlinear bed shear stress, two formulations for the bed shear stress $\vec{\tau}_b$ are employed, i.e. a quadratic formulation

$$\vec{\tau}_b = \rho C_d \vec{u}|\vec{u}|, \tag{9}$$

and a linear formulation

$$\vec{\tau}_b = \rho r \vec{u}. \tag{10}$$

In these expressions, C_d (~ 10^{-3}) is the drag coefficient, and r is the linear friction coefficient given by $r = 8/(3\pi)C_d U_{max}$. The latter expression is derived from Lorentz linearization of the bed shear stress (Zimmerman, 1982). Here U_{max} is the maximum velocity of the basic flow $\vec{u}_0$. Linear and nonlinear bed shear stress were also considered by Roos et al. (2008), but they did not systematically investigate the differences in the resulting growth characteristics of the bedforms.

Regarding sand transport, a bed load formulation is used. Suspended load is not considered, as Besio et al. (2006) found that for coarse sand and a moderate tidal current, the contribution of suspended load to the growth of the bedforms is negligible. The formulation for sand transport used is that of Fredsøe and Deigaard (1992), which is also used in Blondeaux et al. (2009):

$$\vec{q} = \frac{30Q_C}{\mu_d \pi}(\theta - \theta_c)(\sqrt{\theta} - 0.7\sqrt{\theta_c})\left(\frac{\vec{u}}{|\vec{u}|} - \nabla h \cdot \mathbf{G}\right)\mathcal{H}(\theta - \theta_c). \tag{11}$$

Here, $Q_C = \sqrt{(\rho_s/\rho - 1)gd^3}$ is the characteristic sand transport rate, where ρ_s is the density of noncohesive sediment (a relative density $\rho_s/\rho = 2.6$ is used), and d is the uniform grain size. The coefficient μ_d (0.32–0.75) is the dynamic friction coefficient of the bed material. The Shields parameter θ is given by
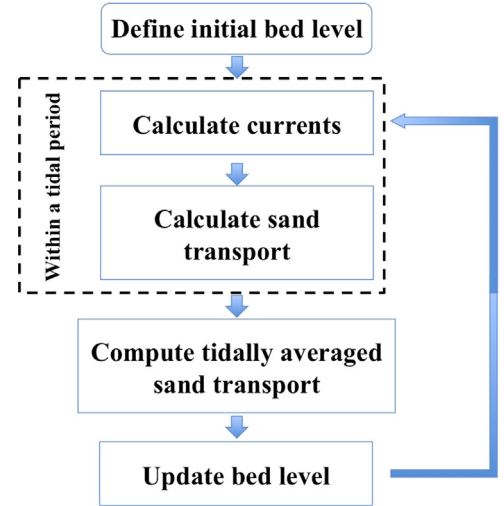

Fig. 3. Flow chart of the numerical model.

$$\theta = \frac{\rho|\vec{u}|^2}{(\rho_s - \rho)gdC'^2}, \tag{12}$$

and θ_c is the critical Shields parameter. The typical value of θ_c ranges between 0.03 and 0.06. For a given θ_c, the critical depth-averaged velocity U_c for sand erosion can be obtained from Eq. (12). Using the Heaviside function $\mathcal{H}$ guarantees that sand transport only takes place when $\theta > \theta_c$. Furthermore, C' is the grain-related conductance coefficient given by $C' = 2.5\ln(11 H/2.5d)$. The dimensionless tensor $\mathbf{G}$ (Seminara, 1998) is related to the slope-induced sand transport. For isotropic sand transport, the tensor $\mathbf{G} = \lambda\mathbf{I}$, where λ is called the bed slope coefficient and $\mathbf{I}$ is the unit tensor. For anisotropic sand transport, in a reference frame (s,n) in which s is aligned with the bed shear stress and n is normal to that direction, the elements of tensor $\mathbf{G}$ read

$$G_{ns} = G_{sn} = 0, \quad G_{ss} = \frac{\theta_c}{\mu_d}\frac{1}{|\vec{q}_0|}\frac{d|\vec{q}_0|}{d\theta}, \quad G_{nn} = \frac{k_G}{\sqrt{\theta}}. \tag{13}$$

Here, $|\vec{q}_0|$ is the modulus of the sand transport rate $\vec{q}$ over a flat bed ($h = 0$ in Eq. (11)), and k_G is an empirical coefficient that has values in the range of 0.5–0.6. By using the expression of θ, $\vec{q}$ is written as

$$\vec{q} = \alpha_e(|\vec{u}|^2 - U_c^2)(|\vec{u}| - 0.7U_c)\left(\frac{\vec{u}}{|\vec{u}|} - \nabla h \cdot \mathbf{G}\right)\mathcal{H}(|\vec{u}| - U_c), \tag{14}$$

where

$$\alpha_e = \frac{30Q_C}{\mu_d \pi}\left(\frac{\rho}{(\rho_s - \rho)gdC'^2}\right)^{\frac{3}{2}}, \quad U_c = \left(\theta_c\left(\frac{\rho_s}{\rho} - 1\right)gd\right)^{\frac{1}{2}}C'. \tag{15}$$

If the critical velocity $U_c = 0$ and isotropic sand transport is considered, Eq. (14) reduces to the formulation as that in Hulscher et al. (1993):

$$\vec{q} = \alpha_e|\vec{u}|^3\left(\frac{\vec{u}}{|\vec{u}|} - \lambda\nabla h\right). \tag{16}$$

2.3. Linear stability analysis

In this study, the initial formation of bedforms is investigated by applying the concepts of linear stability analysis. First, a basic state is defined, which is the spatially uniform tidal current $\vec{u}_0$

Table 1
Overview of the set up of the experiments.

Exp.	Lin/nonlin	Sand transport		Tidal currents		
		U_c (m s^{-1})	Iso/aniso	Constituents	U_{max} (m s^{-1})	ϵ
1	Lin	0	Iso	M_2	1.0	0
2	Nonlin	0	Iso	M_2	1.0	0
3	Lin	0.18:0.2:0.98	Iso	M_2	1.0	0
4	Lin	0	Aniso	M_2	1.0	0
5	Lin	0	Iso	M_2	1.0	$-1{:}0.2{:}1$
6	Lin	0	Iso	K'_1	1.0	0
7	Lin	0	Iso	$M'_2 + K'_1$		0
8	Lin	0	Iso	$M'_2 + S_2$		0
9	Nonlin	0.58	Aniso	M_2	0.6	0.4
10	Lin	0.58	Aniso	M_2	0.6	0.4
11	Nonlin	0.58	Iso	M_2	0.6	0.4
12	Nonlin	0.58	Aniso	M_2	0.61:0.01:0.67	0.4
13	Nonlin	0.58	Aniso	M_2	0.6	$-1{:}0.2{:}1$

In this table, 'lin/nonlin' means linear/nonlinear friction, 'iso/aniso' means isotropic/anisotropic slope-induced sand transport, U_{max} is the maximum velocity of the basic flow $\vec{u}_0$, and ϵ is the tidal ellipticity. The notations with ': ' mean from the first number to the third number with an increment of the middle number. The periods for K'_1 and M'_2 are chosen as 24 h and 12.5 h, respectively.

Table 2
Default values of parameters used in the experiments.

	Parameter	Value	Description
	Ω	7.292×10^{-5} rad s^{-1}	Angular frequency of the Earth
	Φ	52°N	Latitude
	ω_{M_2}	1.40×10^{-4} rad s^{-1}	Angular frequency of M_2 (M'_2) tide
	ω_{S_2}	1.45×10^{-4} rad s^{-1}	Angular frequency of S_2 tide
	$\omega_{K'_1}$	7.27×10^{-5} rad s^{-1}	Angular frequency of K'_1 tide
	g	9.81 m s^{-2}	Gravitational acceleration
	p	0.4	Bed porosity
	λ	2.37	Bed slope coefficient
	μ_d	0.6	Dynamic friction coefficient
	k_G	0.55	Empirical coefficient for aniso-tropic sand transport
Exp. 1–8	H	30 m	Undisturbed water depth
	α_e	2.4×10^{-5} m^{-1} s^2	Coefficient for sand transport
Exp. 9–13	H	40 m	Undisturbed water depth
	d	0.4 mm	Grain size
	θ_c	0.051	Critical Shields parameter

over a flat bottom. After that, small perturbations of the bottom h_0 are introduced, which are periodic in the domain with length and width L_x and L_y:

$$h_0 = h(x, y, 0) = Ae^{i(k_x x + k_y y)} + c.\,c.. \tag{17}$$

In this expression, A is an amplitude that is much smaller than H, k_x and k_y are topographic wavenumbers in the x- and y-directions, and $c.\,c.$ denotes a complex conjugate (the same applies elsewhere). Each h_0 is called a bottom mode. There are two ways to specify the directions of the basic flow and the topographic wave vector of the perturbations. One is to fix the principal direction of the basic flow and vary k_x and k_y. The other is to give a basic flow with varying principal directions and fix the orientation of the crest lines, for instance, by setting the topographic wave vector as $(0, k_y)$ (the crests of the perturbation are along the x-axis). Next, the interaction between the flow and the bottom topography is investigated. According to linear stability theory, since A is small, the solution of the flow and the bed level is written as

$$(u, v, h) = (u_0, v_0, 0) + [(u_1, v_1, h_1)Ae^{i(k_x x + k_y y)} + c.\,c.\,] + O(A^2) \tag{18}$$

Here, $(u_0, v_0, 0)$ is the basic state, and (u_1, v_1, h_1) is the solution at the first order of A. Higher order terms in the solution are neglected. By plugging the solution above in the original governing equations, the linearized equations for (u_1, v_1, h_1) are derived. For a given basic flow, it turns out that each bottom mode evolves as

$$h(x, y, t) = Ae^{\Gamma t}e^{i(k_x x + k_y y)} + c.\,c., \tag{19}$$

with Γ the complex growth rate of the mode, which depends on the topographic wave vector. The real part of Γ is Γ_r, its reciprocal Γ_r^{-1} being the e-folding growth time τ_e of the amplitude of the mode. The mode with the largest Γ_r is called the "fastest growing mode" or the "preferred mode/bedform". The imaginary part Γ_i is the radian frequency of the mode, which is related to the migration speed ($-\Gamma_i/k_x$, $-\Gamma_i/k_y$). As will be shown in Subsection 2.5, the bedforms considered in this study have no migration speed.

2.4. Numerical implementation

The system (Eqs. (4), (5) and (8)), with specific formulations for bed shear stress and sand transport, is solved by using a finite-difference numerical scheme on a regular rectangular staggered grid (Caballeria et al., 2002; Garnier et al., 2006). A central second-order discretization is used in space, while an explicit fourth-order Runge-Kutta scheme is applied for time integration. The explicit scheme needs to satisfy the Courant-Friedrichs-Levy condition, i.e., $\Delta t \leq C \min\{\Delta x, \Delta y\}/\sqrt{gD_{max}}$, where Δt is the time step and $(\Delta x, \Delta y)$ the grid sizes, and D_{max} the maximum water depth. The constant C is determined empirically (generally $C \leq 1.0$). The way of coupling tidal current and sand transport is shown in Fig. 3.

The domain size (L_x, L_y) varies in the range of 1–36 km. Initially, bed perturbations as those in Eq. (17) with a small amplitude A (0.1% of the undisturbed water depth) are imposed on a flat bottom. Details of the basic state and domain size are given in Section 2.5 for different experiments.

Sand transport is calculated after the basic flow has been spun up to a dynamic equilibrium state (the relative tolerance of velocity magnitude at successive tidal cycles is within 0.001%). To calculate the growth rate, the root-mean-square height of the perturbation h_{rms} is computed at the beginning of each tidal cycle, which is defined as

$$h_{rms}(t) = \overline{h\left((x, y, t)^2\right)}^{\frac{1}{2}}. \tag{20}$$
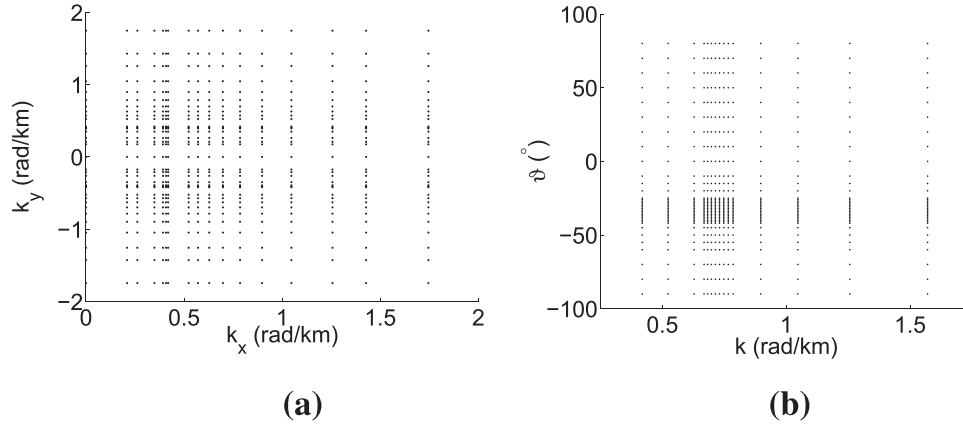
Fig. 4. Sampled parameter space (wavenumbers k_x, k_y of the bottom perturbation and angle ϑ between the principal current direction and the crests): the first configuration (a) and the second one (b). Each dot corresponds to a sampled mode.

Here, the overbar denotes spatial averaging. From Eqs. (17) and (19), it follows that h_{rms} satisfies

$$h_{rms}(t) = h_{rms}(0)e^{\Gamma_r t}. \tag{21}$$

Hence the real part of the growth rate is computed as

$$\Gamma_r = \frac{1}{nT}\ln\left(\frac{h_{rms}(nT)}{h_{rms}(0)}\right). \tag{22}$$

Here, n is an integer that is larger than the number of tidal periods needed for the spin up. At time nT, the term $\ln(h_{rms}(nT)/h_{rms}(0))$ is calculated, and finally the average of Γ_r over several n is taken. Eq. (22) is basically the same as the formulation for calculating Γ_r in Borsje et al. (2013).

2.5. Design of the experiments

Details about the design of the numerical experiments are given in Table 1. Values of the other parameters for the experiments are shown in Table 2. Note that the imposed tidal forcing only includes M_2, K_1, the joint action of $M_2 + K_1$ and $M_2 + S_2$. Migration of the bedforms occurs only if the tidal forcing consists of multiple constituents with angular frequencies that have an integer ratio, for instance, M_2+ residual, $M_2 + M_4$ (Roos et al., 2001; Walgreen et al., 2002). The tidal frequencies of the tidal constituents in this study have non-integer ratios. Hence the bedforms driven by these tidal constituents do not migrate, and the focus here is on the real part of the growth rate Γ_r.

First, to check if the model is capable of reproducing the initial formation of tidal sand ridges, the same parameter values and formulations for sand transport and bottom friction as those in Hulscher et al. (1993) (Exp. 1) are used. Next, the effect of nonlinear bed shear stress on the characteristics (growth rate, wavelength and orientation) of the preferred bedforms during their initial formation is studied in Exp. 2. Furthermore, using Eq. (14), a critical depth-averaged velocity U_c for sand erosion and anisotropic slope-induced sand transport are considered in Exps. 3 and 4, respectively. Decreasing U_c means either decreasing grain size or assuming an increase in stirring of sand by waves. In this study, the latter interpretation applies since the grain size is assumed to be kept as a constant. In the experiments hereafter, tidal currents with different characteristics are considered: elliptical tidal currents in Exp. 5, the diurnal tide in Exp. 6, the mixed semidiurnal tide in Exp. 7, and the spring-neap tide in Exp. 8. To reduce the computation time, in Exp. 7 the periods of the M_2 tide and the K_1 tide are adjusted slightly (denoted by M'_2 and K'_1, respectively). The same applies to Exp. 8, in which the adjusted M'_2 tide is used. In the cases of a mixed tide and a spring-neap tide, the tidal constituents are chosen to have the same phase and inclination. For the mixed tide, the velocity amplitude of the M'_2 tide $U_{M'_2} = 1$ m s^{-1}, while the velocity amplitude of the K'_1 tide $U_{K'_1}$ increases from 0.1 m s^{-1} to 0.5 m s^{-1}. For the spring-neap tide, the velocity amplitudes of the tidal constituents are chosen such that the representative amplitude $U_r = (U_{M'_2}^2 + U_{S'_1}^2)^{1/2}$ is kept at 1 m s^{-1}.

To verify whether the present model yields long bed waves if both the elliptical tide and critical velocity are included, Exp. 9 is conducted. The same parameter values (Tables 1,2) and formulations as in Blondeaux et al. (2009) are used. The drag coefficient is
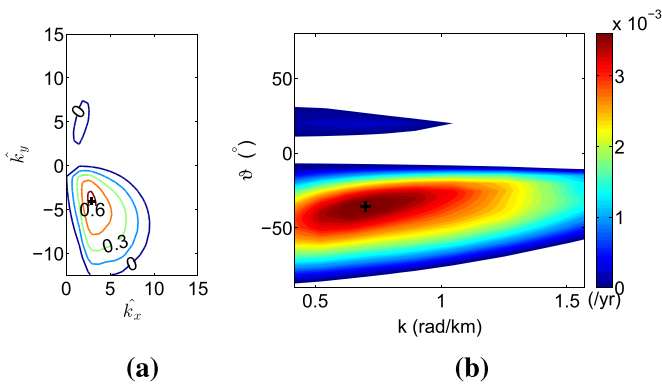
Fig. 5. Exp. 1: (a) Dimensionless growth rate of the bed perturbations as a function of the dimensionless wavenumbers; (b) dimensional growth rate Γ_r as a function of dimensional wavenumber k and angle ϑ between the principal current direction and the crests of the bed perturbations. The plus corresponds to the fastest growing mode.
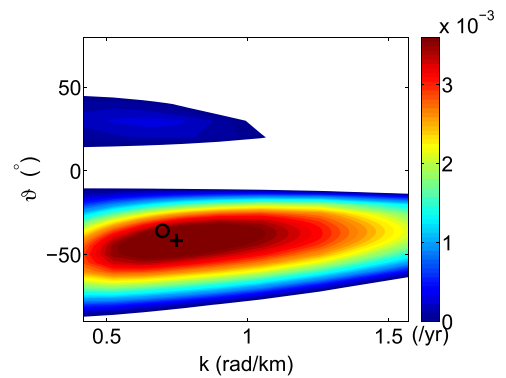
Fig. 6. Growth rate Γ_r of the bed perturbations as a function of wavenumber k and angle ϑ between the principal current direction and the crests of the bed perturbations, using nonlinear bed shear stress (Exp. 2). The plus and circle correspond to the fastest growing modes using nonlinear shear stress (Exp. 2) and linearized stress (Exp. 1), respectively.

calculated by $C_d = \left(2.5\ln\left(11\tilde{D}/z_r \right) \right)^{-2}$, where z_r is the roughness of the sea bottom and a value of 2.5 cm is taken. In addition, the sensitivity of the formation of long bed waves to the linearized/nonlinear bed shear stress (Exp. 10), isotropic/anisotropic slope-induced sand transport (Exp. 11), maximum current velocity (Exp. 12), and the ellipticity of tidal current (Exp. 13) is examined. In the experiments with anisotropic sand transport, the bed slope coefficients are calculated from Eq. (13).

In Exp. 1, two ways of specifying the directions of the basic flow and bottom perturbations are used. In the first configuration, the principal direction of the basic tidal current is parallel to the x-direction, and the wavenumbers of the perturbation are chosen as $k_x = 2\pi/L_x$ and $k_y = 2\pi/L_y$, where L_x and L_y are the length of the domain in the x- and y-directions, respectively. The sampled wavenumbers are shown in Fig. 4a. This is done in order to allow for straightforward comparison of model results with those of Hulscher et al. (1993). In the second one, it is configured such that the wavelength and orientation of the fastest growing mode can be accurately identified: the direction of the basic flow is varied between $-90°$ and $90°$, and the bottom modes have wavenumbers $(0, k_y)$ $(k_y = k = 2\pi/L_y)$. First a relatively low resolution in the (ϑ, k) space is used, possible later refinement is done after analysis of these results. Since the crests of the perturbation are aligned along the x-axis ($k_x = 0$), ϑ also indicates the angle between the principal current direction and the crests. Positive/negative ϑ means that the crests are rotated anticyclonically/cyclonically with respect to the principal current direction in the Northern Hemisphere. Hereafter, whenever the orientation of the mode/crests is mentioned, it is always with respect to the principal current direction, and its absolute value is used when the orientation of the mode is compared between experiments. The second configuration is used in all other experiments. The sampled parameter space of Exp. 1 using the second configuration is shown in Fig. 4b. Generally, near the fastest growing mode, the resolution in ϑ is within 1° (up to 0.2°), and in
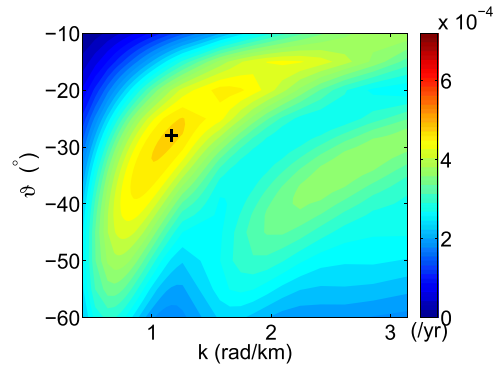

Fig. 8. Growth rate Γ_r of the bed perturbations as a function of wavenumber k and angle ϑ between the principal current direction and the crests of the bed perturbations, with the critical depth-averaged velocity U_c for sand erosion equal to 0.98 m s^{-1} (Exp. 3). The plus corresponds to the fastest growing mode.

the wavelength it is around 200 m for Exp. 1–8 (the grid sizes are $\Delta x = \Delta y = 200$ m, with a time step $\Delta t = 10$ s) and 100 m for the rest experiments (the grid sizes are $\Delta x = \Delta y = 100$ m, with a time step $\Delta t = 5$ s). Tests have shown that if the modes have a wavenumber $(0, k_y)$, the domain length in the x-direction L_x does not affect the growth rate of the modes. Hence L_x is chosen equal to $3\Delta x$, which is the minimum possible value.

3. Results

3.1. Verification with Hulscher et al. (1993)

First the present model is run using the same configuration and parameter values as those used in Hulscher et al. (1993) (Exp. 1 in Table 1). Fig. 5a shows a contour plot of the dimensionless growth rate $\hat{\Gamma}_r$ of the bed perturbations versus dimensionless
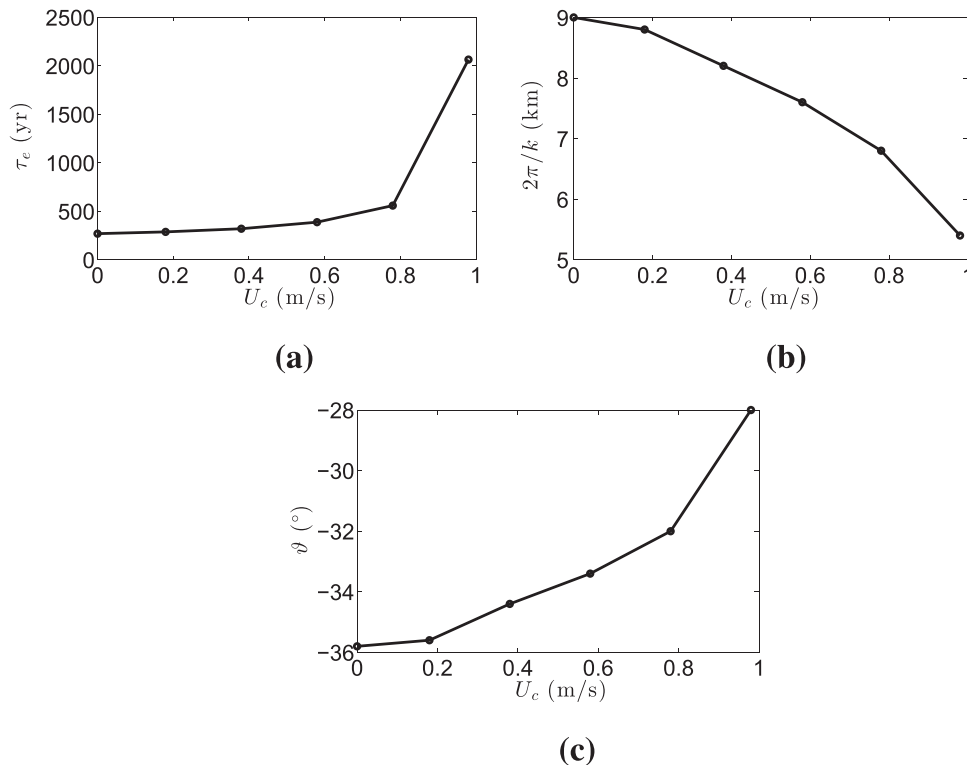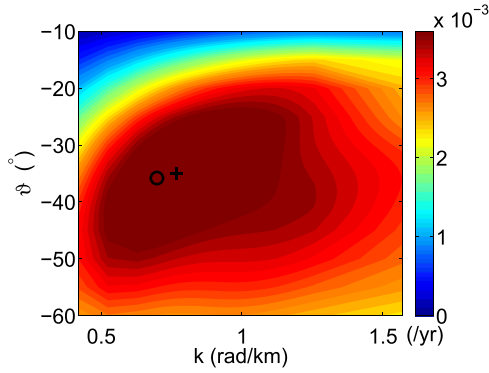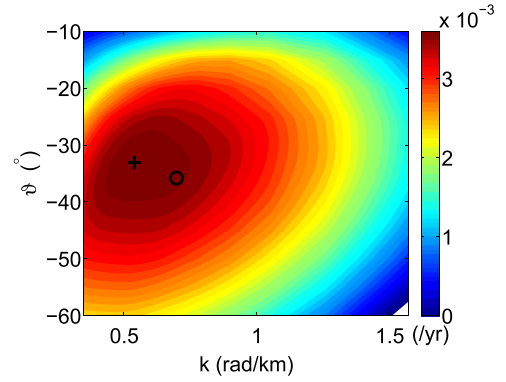

(a)

(b)

(c)

Fig. 7. (a) The e-folding time τ_e, (b) wavelength $2\pi/k$ and (c) orientation angle ϑ of the fastest growing mode as a function of the critical depth-averaged velocity U_c for sand erosion (Exp. 3).

Fig. 9. Growth rate Γ_r of the bed perturbations as a function of wavenumber k and angle ϑ between the principal current direction and the crests of the bed perturbations, using anisotropic slope-induced sand transport (Exp. 4). The plus and circle correspond to the fastest growing modes using anisotropic (Exp. 4) and isotropic sand transport (Exp. 1), respectively.


Fig. 11. Growth rate Γ_r of the bed perturbations as a function of wavenumber k and angle ϑ between the principal current direction and the crests of the bed perturbations, using the K'_1 tide (Exp. 6). The plus and circle correspond to the fastest growing modes using K'_1 (Exp. 6) and M_2 (Exp. 1), respectively.

wavenumbers $\hat{k}_x$ ($\hat{k}_x = k_x U_{max}/\omega$) and $\hat{k}_y$ ($\hat{k}_y = k_y U_{max}/\omega$). In this configuration, the principal direction of the basic flow is along the x-axis, as in Hulscher et al. (1993). Here, $\hat{\Gamma}_r = T_m \Gamma_r$, where $T_m = (1 - p)H/(\alpha_e U_{max}^2 \omega)$ is the morphological time scale. For $H = 30$ m, $U_{max} = 1$ m s^{-1}, $\omega = 1.4 \times 10^{-4}$ rad s^{-1}, $p = 0.4$ and $\alpha_e = 2.4 \times 10^{-5}$ m^{-1} s^2, $T_m \approx 170$ years. In Fig. 5b, the results are shown in a different way, i.e., dimensional growth rate Γ_r as a function of dimensional wavenumber k and angle ϑ between the principal current direction and the crests (parallel to the x-direction) of the bed perturbation. Growing modes (modes with positive growth rate Γ_r) with different orientations are observed, i.e., their crests are either cyclonically or anticyclonically rotated with respect to the principal direction of the tidal current. From Fig. 5, it is seen that the fastest growing mode has a dimensionless wavenumber of 5.0 and a dimensional wavenumber of ~0.7 rad km^{-1}, which is equivalent to a dimensional wavelength of 9.0 km.

Furthermore, the direction of the crests is approximately 35.8° cyclonically oriented with respect to the principal current direction. The obtained wavelength and the angle between the principal current direction and the crests of the fastest growing mode are larger than those in Hulscher et al. (1993) (wavelength approximately 8 km and $|\vartheta|$ approximately 30°). The e-folding time scale τ_e ($\tau_e = \Gamma_r^{-1}$) is 270 years, while it is around 400 years in Hulscher et al. (1993). Possible reasons for these differences will be discussed in Section 4.

3.2. Nonlinear bed shear stress

For the case using a nonlinear bed shear stress (Exp. 2), the growth rate of the bed perturbations as a function of dimensional wavenumber k and angle ϑ between the principal current direction and the crests of the bed perturbation is shown in Fig. 6. The fastest growing mode has a smaller e-folding time ($\tau_e \approx 250$ years)
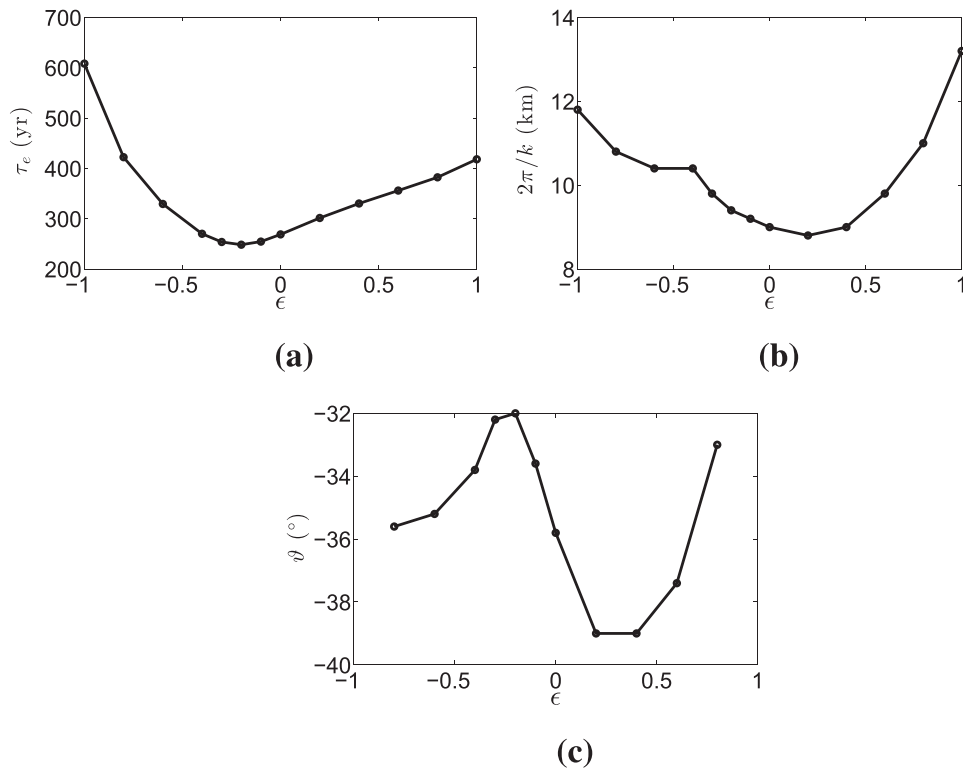
Fig. 10. (a) The e-folding time τ_e, (b) wavelength $2\pi/k$ and (c) orientation angle ϑ of the fastest growing mode as a function of tidal ellipticity ϵ (Exp. 5).
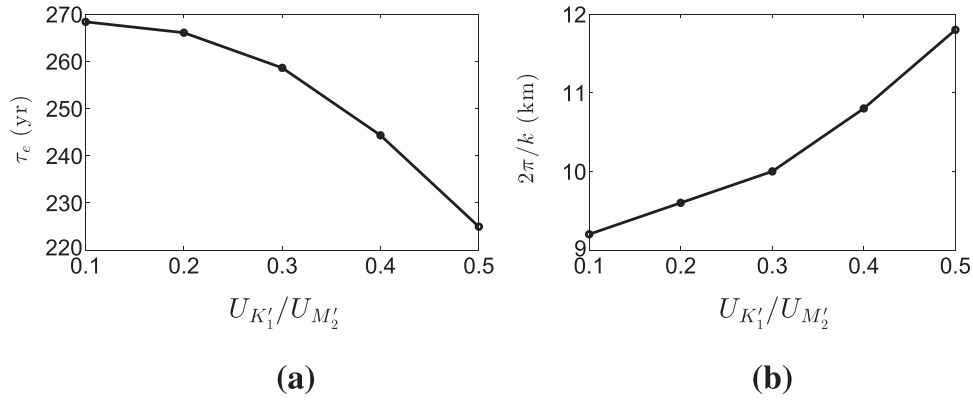
Fig. 12. (a) The e-folding time τ_e and (b) wavelength $2\pi/k$ of the fastest growing mode as a function of $U_{K'1}/U_{M'2}$ (Exp. 7).

and a slightly smaller wavelength (~ 8.4 km) than that obtained if a linearized bed shear stress is used, while the absolute value of the angle ($\sim 41.8°$) between the principal current direction and the crests becomes larger.

3.3. Critical bed shear stress for sand erosion

Fig. 7 shows the e-folding time, wavelength and orientation of the fastest growing mode versus the critical depth-averaged velocity for sand erosion U_c (Exp. 3). In general, the e-folding time of the fastest growing mode increases as the critical velocity increases. Moreover, the wavelength and the absolute value of the angle between the principal current direction and the crests decrease with increasing U_c. For $U_c = 0.58$ m s^{-1}, the e-folding time of the fastest growing mode ($\tau_e \approx 390$ years) increases more than 31% of that if the threshold is not considered (Fig. 7a), and the wavelength decreases by around 1.4 km (Fig. 7b). The change in the orientation angle is less significant until U_c reaches 0.78 m s^{-1} (Fig. 7c).

Note that once the critical velocity is close to the maximum current velocity (Fig. 8), the growth rate decreases significantly and the maxima are found not only near the wavelength of 5.4 km with $\vartheta \sim -28°$, but also around 2.4 km with $\vartheta \sim -34°$. The latter parameters are representative for long bed waves, since the wavelength is between those of sand waves and tidal sand ridges, albeit that the orientation angle found here differs from the observations (approximately $-60°$ or $30°$).

3.4. Anisotropic slope-induced sand transport

The growth rate of the bed perturbations in Exp. 4 using anisotropic slope-induced sand transport is shown in Fig. 9. Compared to the case using isotropic slope-induced sand transport
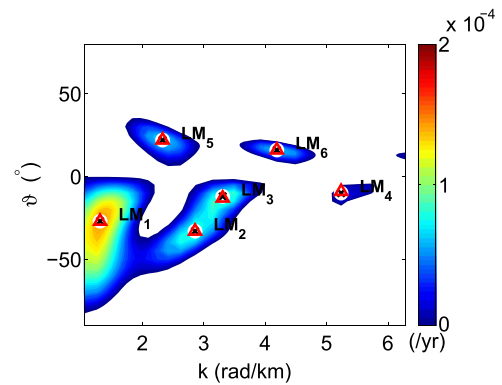

Fig. 14. Growth rate Γ_r of the bed perturbations as a function of wavenumber k and angle ϑ between the principal current direction and the crests of the bed perturbations, with both critical bed shear stress and elliptical tides (Exp. 9). Local maxima are marked by the crosses in the white circles, and are named as LM_1 to LM_6. The triangles indicate the local maxima found by Blondeaux et al. (2009).

(Exp. 1), the fastest growing mode has a slightly smaller e-folding time ($\tau_e \approx 250$ years) and a smaller wavelength (~ 8.2 km). The orientation of the fastest growing mode hardly changes.

3.5. Tidal ellipticity

The e-folding time, wavelength and orientation of the fastest growing mode against tidal ellipticity ε (Exp. 5) are shown in Fig. 10. The e-folding time of the fastest growing mode using circular tides is approximately 1.3 ($\varepsilon = 1$) and 2 ($\varepsilon = -1$) times of that using a rectilinear tide. Note that the smallest e-folding time of the fastest growing modes along ε is not found at $\varepsilon = 0$, but rather near $\varepsilon = -0.2$. The wavelength of the fastest growing mode does not change much for $-0.3 \leq \varepsilon \leq 0.4$, and the smallest wavelength is
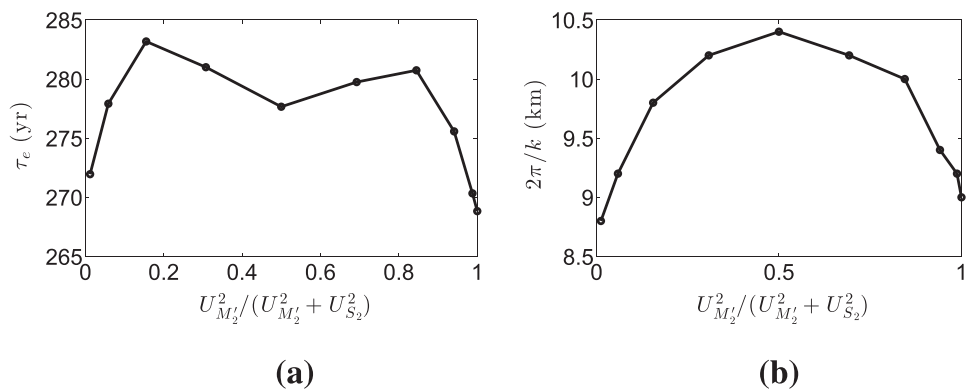

Fig. 13. (a) The e-folding time τ_e and (b) wavelength $2\pi/k$ of the fastest growing mode as a function of $U^2_{M'2}/(U^2_{M'2} + U^2_{S_2})$ (Exp. 8).

observed near $\varepsilon = 0.2$. It increases as the absolute value of ε increases for $|\varepsilon| > 0.4$. The orientation angle of the fastest growing mode also depends non-monotonically on the tidal ellipticity. The absolute value of ϑ decreases from $\varepsilon = -0.8$ to $\varepsilon = -0.2$, next increases rapidly until $\varepsilon = 0.2$ and decreases again towards $\varepsilon = 0.8$. Note that for $\varepsilon = \pm 1$, the growth rates of the perturbation are independent of the angle ϑ, thus in Fig. 10c no data are shown for $\varepsilon = \pm 1$.

3.6. Diurnal tide

Fig. 11 shows a contour plot of the growth rate of the bed perturbations using a diurnal tide K'_1 (Exp. 6). Compared to the result in Exp. 1, it is found that the *e*-folding time of the fastest growing mode using a diurnal tide hardly changes. Furthermore, it is seen that the fastest growing mode using the K'_1 tide has a smaller wavenumber (equivalently the wavelength increases by around 3 km) and a smaller orientation angle (around 3° smaller) than that using the M_2 tide.

3.7. Mixed tide and spring-neap tide

Fig. 12 shows the *e*-folding time and wavelength of the fastest growing modes against the ratio of the velocity amplitude of the K'_1 tide and the M'_2 tide (Exp. 7). If $U_{M'_2}$ is fixed, it is found that as the ratio $U_{K'_1}/U_{M'_2}$ increases from 0.1 to 0.5, the *e*-folding time of the fastest growing modes decreases (Fig. 12a) by approximately 40 years, while the wavelength of the fastest growing modes increases (Fig. 12b) by 2.6 km. The orientation angles of the fastest growing modes are between $-36°$ and $-35°$ (not shown). The results of additional experiments show that phase difference between tide K'_1 and tide M'_2 has no effect on the growth rate, wavelength and orientation of the fastest growing modes.

In Fig. 13, the *e*-folding time and wavelength of the fastest growing modes are plotted against the ratio between the squared

velocity amplitude of the M'_2 tide and the squared representative velocity (Exp. 8). It appears that the dependency of the *e*-folding time of the fastest growing modes (Fig. 13a) on this parameter is rather weak (changes are less than 15 years). In contrast, the wavelength of the fastest growing modes (Fig. 13b) increases by around 1.4 km when the ratio $U_{M'_2}^2/(U_{M'_2}^2 + U_{S_2}^2)$ increases from 0 to 0.5, i.e., from the S_2 tide dominant to $U_{M'_2} = U_{S_2}$. The change of the orientation angles is within 1° (not shown). Like in the case of the mixed tides, the phase difference between the M'_2 tide and the S_2 tide does not affect the characteristics of the fastest growing modes. The variations in the growth rate and the wavelength of the preferred bedforms for the mixed tides and spring-neap tides reveal that the characteristics of these bedforms are determined by the dominant tidal constituent.

3.8. Combined tidal ellipticity and critical velocity for sand erosion

The combination of tidal ellipticity and critical shear stress is considered in Exp. 9. The drag coefficient was calculated using the same formulation as that of Blondeaux et al. (2009), i.e., $C_d = \left(2.5\ln\left(11\tilde{D}/z_r\right)\right)^{-2}$, where $z_r = 2.5$ cm is the roughness of the sea bottom. In that case, the morphological time scale, for the given sand transport formulation and parameters, is $T_m \sim 500$ years. The result is shown in Fig. 14, in which several local maxima in the growth rate Γ_r (LM$_1$ to LM$_6$) with both positive and negative orientation angles are observed. The maximum in Γ_r with the smallest wavenumber LM$_1$ is identified at $k \sim 1.30$ rad/km and $\vartheta \sim -27°$, the corresponding *e*-folding time is around 13 times of the morphological time T_m. This is related to the tidal sand ridge mode that has a wavelength of around 4.8 km and crests that are $\sim 27°$ cyclonically oriented with respect to the principal current direction. The other local maxima in Γ_r occur for wavenumbers that correspond to those of long bed waves modes (wavelengths are in the range of 1–3 km). Two local maxima in Γ_r with negative
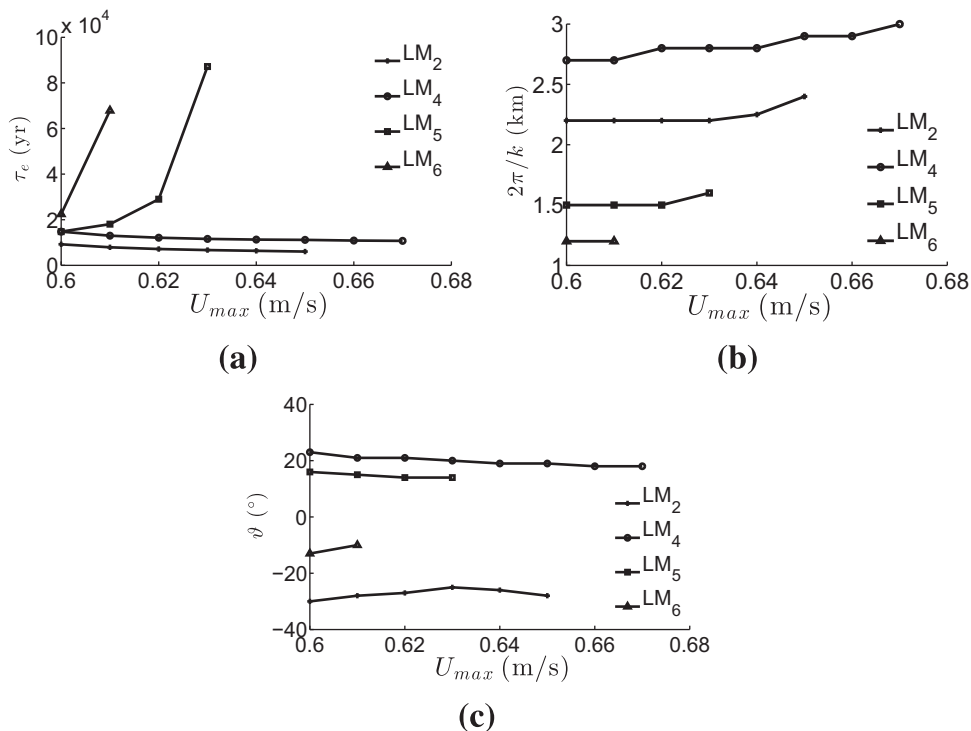

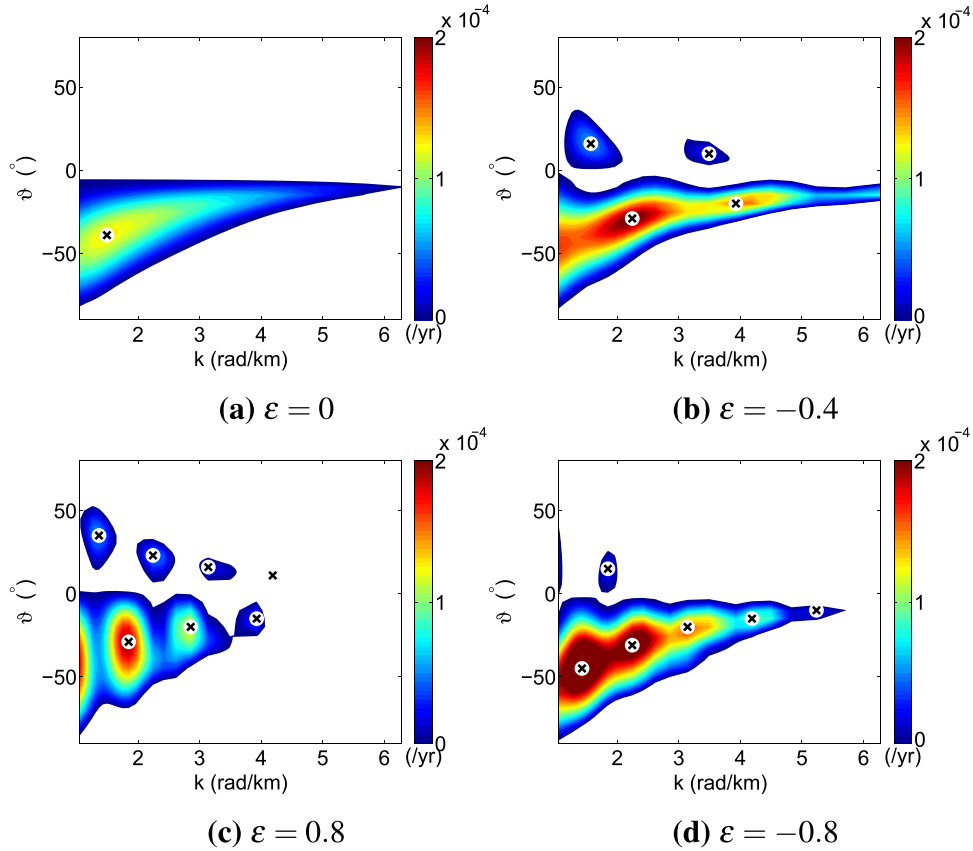**Fig. 15.** (a) The *e*-folding time τ_e, (b) wavelength $2\pi/k$ and (c) orientation angle ϑ of the local maxima (LM$_2$, LM$_4$, LM$_5$ and LM$_6$ as shown in Fig. 14) as a function of the maximum current velocity U_{max} (Exp. 12).

Fig. 16. Growth rate Γ_r of the bed perturbations as a function of wavenumber k and angle ϑ between the principal current direction and the crests of the bed perturbations, for different values of tidal ellipticity (Exp. 13). The crosses in the white circles correspond to local maxima in Γ_r.

ϑ, LM_2 and LM_3, are observed at a wavelength of around 2 km. One is found at $k \sim 2.9$ rad/km (wavelength around 2.2 km) and $\vartheta \sim -33°$, and the other at $k \sim 3.3$ rad/km (wavelength around 1.9 km) and $\vartheta \sim -13°$. Another long bed wave mode with negative ϑ, LM_4, is found at $k \sim 5.2$ rad/km (wavelength around 1.2 km) and $\vartheta \sim -11°$. For $\vartheta > 0°$, LM_5 occurs at $k \sim 2.4$ rad/km (wavelength around 2.7 km) and $\vartheta \sim 22°$, and LM_6 is found at $k \sim 4.2$ rad/km (wavelength around 1.5 km) with $\vartheta \sim 16°$. The e-folding times of the long bed wave modes from LM_2 to LM_6 are approximately 23, 22, 70, 30 and 29 times of the morphological time T_m, respectively. The wavelength and orientation of the local maxima agree quite well with those in Blondeaux et al. (2009). Generally, the

differences in the e-folding times between the present results and those of Blondeaux et al. (2009) are within 15%. The reason for the differences is given in Section 4.

3.9. Key parameters for the initial formation of long bed waves

The results above demonstrate the ability of the present numerical model to simulate the initial formation of long bed waves. An additional experiment using a constant drag coefficient of 0.003 gives similar wavelength, orientation and growth rate of the local maxima as in Exp. 9 (not shown). To further test the essential conditions under which long bed waves form, experiments (Exp.
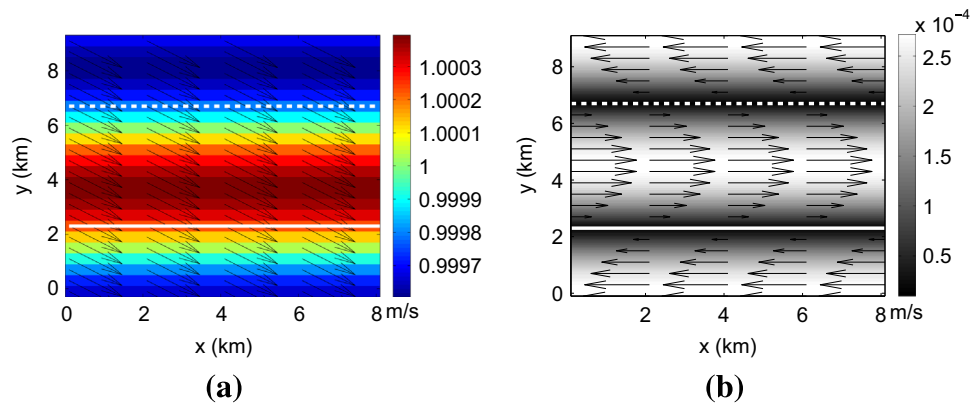
Fig. 17. Tidal current patterns for the preferred bedform in Exp. 1. The solid/dashed line stands for the crest/trough of the bed perturbation. The principal direction of the basic flow is 35.8° clockwise rotated with respect to the x-axis. (a) Total tidal current during flood. The colormap/arrow indicates the magnitude/vector of the tidal current. Note that the current velocity is larger upstream of the crest and smaller downstream of the crest, which also occurs during ebb. (b) The residual current, with the colormap/arrow indicating its magnitude/vector. Note that the residual current is anticyclonic around the crest, and its magnitude is small because the amplitude of the bedform is small.

10–13) were carried out in which linearized bed shear stress, isotropic sand transport, different values of maximum current velocity and tidal ellipticity were considered. A constant drag coefficient of 0.003 was used in those experiments except in Exp. 10, in which a linear friction coefficient $r = 1.5 \times 10^{-3}$ m s^{-1} was employed, obtained from $r = 8/(3\pi)C_d U_{max}$.

The linearized bed shear stress (Exp. 10) causes only minor changes in the wavenumber and orientation of the local maxima in Γ_r that correspond to long bed waves (not shown). The growth rates of anticyclonically oriented long bed wave modes (LM$_5$ and LM$_6$ as shown in Fig. 14) become almost twice of those using nonlinear bed shear stress, while for cyclonically oriented modes, the change in the growth rate is negligible.

For isotropic sand transport (Exp. 11), long bed waves (LM$_2$, LM$_5$ and LM$_6$) with similar wavelengths and orientations are observed compared to those using anisotropic sand transport (not shown). Another long bed wave mode with the same wavelength as LM$_4$ in the anisotropic sand transport case but much larger absolute value of the orientation angle ($\vartheta \sim -40°$) is identified. Besides, a cyclonically oriented long bed wave mode with a wavelength of 1.3 km ($\vartheta \sim -25°$) is observed instead of the mode LM$_3$. In general, the growth rates of the long bed wave modes with isotropic sand transport (LM$_2$, LM$_5$ and LM$_6$) are a factor of about 1.6 times larger than those with anisotropic sand transport. Note that the difference in the e-folding time between LM$_2$ and LM$_1$ is within 100 years when isotropic sand transport is used, which means that long bed waves and tidal sand ridges could emerge on the same time scale.

The variations of the e-folding time τ_e, wavelength $2\pi/k$ and orientation angle ϑ of several long bed wave modes (LM$_2$, LM$_4$, LM$_5$ and LM$_6$ as shown in Fig. 14) along the maximum current velocity U_{max} are shown in Fig. 15 (Exp. 12). It is seen from Fig. 15 that as U_{max} increases, the e-folding time (Fig. 15a) decreases for the modes with larger wavelengths (LM$_2$ and LM$_4$), while it increases for the modes LM$_5$ and LM$_6$. The wavelengths of all the modes except LM$_6$ become larger (Fig. 15b), and the number of the long bed wave modes decreases with an increasing U_{max}: LM$_6$ disappears at $U_{max} = 0.62$ m s^{-1} and LM$_5$ at $U_{max} = 0.64$ m s^{-1}, followed by LM$_2$ at $U_{max} = 0.66$ m s^{-1}. The change in the orientation of the modes is subtle (Fig. 15c). The anticyclonically oriented mode LM$_4$ has a wavelength of 3 km at $U_{max} = 0.67$ m s^{-1}, hence it could still be considered as a long bed wave mode. However, it may not be identified as a long bed wave anymore if U_{max} keeps increasing, as the wavelength of the mode will increase accordingly.

Fig. 16 (Exp. 13) shows the growth rate of the bed perturbations for different values of tidal ellipticity. A maximum (wavelength around 4.2 km) related to tidal sand ridge is seen from Fig. 16a for a rectilinear tide. When $\varepsilon = -0.4$ (Fig. 16b), three long bed wave modes are observed: two cyclonically oriented modes at $k \sim 2.2$ rad/km and $\vartheta \sim -29°$, and $k \sim 3.9$ rad/km and $\vartheta \sim -20°$, and an anticyclonically oriented mode at $k \sim 3.5$ rad/km and $\vartheta \sim 10°$. Fig. 16c shows that more anticyclonically oriented long bed waves ($k \sim 2.2$ rad/km and $\vartheta \sim 23°$, $k \sim 3.1$ rad/km and $\vartheta \sim 16°$, and $k \sim 4.2$ rad/km and $\vartheta \sim 11°$) appear when the tidal ellipticity is large and positive. In contrast, more cyclonically oriented long bed waves ($k \sim 2.2$ rad/km and $\vartheta \sim -31°$, $k \sim 3.1$ rad/km and $\vartheta \sim -20°$, $k \sim 4.2$ rad/km and $\vartheta \sim -15°$ and $k \sim 5.2$ rad/km and $\vartheta \sim -10°$) are found when the tidal ellipticity is negative and its absolute value is large (Fig. 16d). Moreover, it is seen from Figs. 16b and d that for anticyclonic tides, as the absolute value of tidal ellipticity increases, the growth rate increases significantly for cyclonically oriented long bed waves, while it decreases for anticyclonically oriented long bed waves.

4. Discussion

4.1. Mechanism of the formation of large-scale bedforms

The physical mechanisms causing the initial formation of tidal sand ridges and long bed waves have been discussed in several studies. Among many of the hypotheses, linear stability theory has been proven to be successful in explaining the characteristics of observed bedforms, which is also supported by the results in this study. The crucial aspect for both types of bedforms is the joint action of the background tidal current and the residual current that is generated by tide-topography interaction.

Regarding tidal sand ridges, Zimmerman (1981) used vorticity concepts to show that for a ridge that is obliquely oriented with respected to the tidal current, the frictional torque generates a residual current that acts with the tidal current on the upstream side of the ridges, whilst it acts against the tidal current on the downstream side (Fig. 17). The intensity of this residual current is maximum if the distance between successive ridges is of the order of the tidal excursion length U/ω (the distance traveled by particles in one tidal period). Here, U and ω are the characteristic current velocity amplitude and radian tidal frequency, respectively. As explained by Huthnance (1982), since advective sand transport induced by the flow increases faster than linearly with the instantaneous current, sand transport on the upstream side is larger than that on the downstream side. In the case of a symmetric tidal current, this results in net accumulation of sand at the crest. On the other hand, the sand transport due to local bed slopes is directed downslope, thus this transport is divergent at the crests, which increases if ridges are spaced closer together (larger wavenumber k). The competition between advective and slope-induced sand transport gives rise to a fastest growing mode with a certain wavelength and orientation. In addition, if Coriolis torque is considered, it generates a residual flow in the same direction as that due to the frictional torque if the ridge is oriented cyclonically with respect to the tidal current. The opposite occurs if the ridge has an anticyclonic orientation with respect to the tidal current. Thus, convergence of advective sand transport at the crest is larger than that in the former case. This explains the preferred cyclonic orientation of tidal sand ridges. In the case of an asymmetrical tidal current, Roos et al. (2001) and Walgreen et al. (2002) have shown that a flood-dominant current (the maximum flood current is larger than the maximum ebb current) causes convergence of advective sand transport to occur downstream of the crests, thereby affecting the growth of the ridges and causing the ridges to move downstream. If the current is ebb-dominant, i.e., the maximum ebb current is larger than the maximum flood current, the ridges migrate upstream.

Concerning long bed waves, it was demonstrated by Blondeaux et al. (2009) that they form if sand transport takes place during only part of the tidal cycle (tidal current amplitude slightly above the critical velocity for sand erosion) and the tidal current is elliptical. In those cases, the growth or decay of bedforms is determined by the joint action of the tidal current and the residual current that is calculated over the interval that the bed is active. For cyclonically oriented bedforms, the residual current is anticyclonic due to the combined effect of friction torque and Coriolis torque. The residual current around anticyclonically oriented bedforms is generally weaker than that around cyclonically oriented bedforms. However, the residual current computed over the interval that the bed is active can be in the same order as that for cyclonically oriented bedforms and be cyclonic. As a result, bedforms with either cyclonic or anticyclonic orientation with respect to the tidal current occur.

4.2. Differences between present results and those in previous

studies

Comparing the results of Exp. 1 (Fig. 5) with those in Hulscher et al. (1993), it turns out that the growth rate, wavelength and angle between the principal current direction and the crests of the fastest growing mode from the present model are slightly larger. The difference is caused by two reasons. First, Hulscher et al. (1993) used a harmonic truncation of the perturbed flow, in which the cut off was taken place after the second overtide of the principal M_2 constituent. In contrast, since the upper limit frequency of the harmonic components is determined by the time step in a numerical model, many more harmonic components generated by the basic current are included automatically in the present model. Second, Hulscher et al. (1993) neglected the $\partial \zeta / \partial t$ term in the continuity equation (rigid-lid approximation).

Comparison between the results in Exp. 9 (Fig. 14) and those in Blondeaux et al. (2009) shows marginal differences in the wavelength and orientation of the preferred bedforms, though slight differences in the growth rate are observed. The differences are attributed to the fact that the rigid lid approximation was used in their study, whereas the surface elevation $\tilde{\zeta}$ varies in time and space in the present model.

4.3. Key parameters for the initial formation of offshore large-scale bedforms

Several parameters have been varied in this study to investigate whether they are essential for the initial formation of tidal sand ridges and long bed waves, i.e., linear versus nonlinear bottom friction, critical velocity for sand erosion, isotropic versus anisotropic slope-induced sand transport, tidal ellipticity and different tidal constituents.

Nonlinear bed shear stress is neither crucial for the generation of tidal sand ridges (Fig. 6 in Exp. 2), nor for long bed waves (compare Exp. 9 with Exp. 10). Likewise, the anisotropic slope-induced sand transport is not crucial for the formation of the bedforms, albeit that the growth rate of the preferred bedforms is sensitive to the formulations of the slope-induced sand transport (Fig. 9 in Exp. 4, and compare Exp. 9 with Exp. 11). Compared to the case using linear bed shear stress, using nonlinear bed shear stress generates friction torques with slightly different values, thereby giving rise to a different residual current, and further different advective sand transport. If anisotropic slope-induced sand transport is used, the coefficients for the slope-induced sand transport change, hence different divergent sand transport is obtained compared to the case in which isotropic slope-induced sand transport is used.

Critical velocity for sand erosion (Fig. 8 in Exp. 3 and Fig. 15 in Exp. 12) is crucial for the generation of long bed waves: the critical velocity should be slightly smaller than the maximum flow velocity. If the critical velocity is considered, the tidal current and the residual current in a tidal period are the same as that in the case in which the critical velocity is absent ($U_c=0$). However, the net sand transport occurs only during the time that the bed is active. Hence both the advective and slope-induced sand transport differ from that in the case $U_c=0$. If an elliptical tide instead of a rectilinear tide is considered (Fig. 10 in Exp. 5 and Fig. 16 in Exp. 13), both the advective and slope-induced sand transport change, which is due to the change in the tidal current and the residual current.

Different tidal constituents are not essential for the generation of the offshore tidal sand ridges. Nevertheless, compared to the case using only the principal semidiurnal tide, due to the change of the tidal current and the residual current, the advective and slope-induced sand transport alter accordingly. Hence bedforms with different characteristics appear, as has been seen from the results of the experiments with the diurnal tide (Fig. 11 in Exp. 6), the

mixed tide (Fig. 12 in Exp. 7) and the spring-neap tide (Fig. 13 in Exp. 8).

4.4. Comparison with field data

In the southern North Sea, tidal sand ridges with different characteristics are observed (Fig. 1). The focus here is on the Dutch Banks and the Flemish Banks. The Norfolk Banks will be considered in further research.

Although the areas of the Dutch Banks and the Flemish Banks are characterized by the same mean water depth, compared to the Flemish Banks, the Dutch Banks have a larger wavelength. From Roos et al. (2004), the wavelength of the Dutch Banks is in the range of 5.7–9.8 km, and the orientation angle is $-25°$; near the Flemish Banks, the wavelength of the ridges is around 4.5 km, and the orientation angle is $-6°$. To explain the different appearance of the ridges mentioned above, several experiments were conducted, i.e., with/without elliptical tide and with/without critical velocity for sand erosion.

Topography, tidal conditions and the grain size information are based on those from Roos et al. (2004) and van Santen et al. (2011). In the model, a mean water depth of 29 m is used. At the Dutch Banks, the maximum velocity of the M_2 tide is chosen as 0.75 m s^{-1} with an ellipticity of -0.2, and the grain size is 0.25 mm. At the Flemish Banks, a stronger current with a velocity amplitude of 0.8 m s^{-1} and an ellipticity of 0.1 is employed, and the sand is coarser (0.45 mm). Using $\theta_c = 0.05$ yields values of the critical velocity for sand erosion U_c of 0.46 m s^{-1} and 0.59 m s^{-1} in the areas of the Dutch Banks and the Flemish Banks, respectively. A nonlinear bed shear stress with a constant drag coefficient C_d of 0.003 is used. The sand transport is calculated from Eq. (14), in which the parameters μ_d, K_G and ρ_s/ρ have the same values as those in Exp. 9. The modeled preferred bedforms in the areas of the Dutch Banks and the Flemish Banks have a wavelength of around 6.0 km and 5.2 km, respectively, which qualitatively agree with the observations. The e-folding times of the preferred bedforms are around 600 years at both locations. If the critical velocity $U_c=0$ and the ellipticity is kept the same as above, the wavelength of the preferred bedforms changes to 7.0 km for the Dutch Banks and 6.4 km for the Flemish Banks, and the e-folding time decreases to 360 years and 280 years, respectively. Furthermore, if the critical velocity is included and rectilinear tides are used, the wavelengths of the preferred bedforms at both locations become 5.4 km, and the change in the e-folding time is within 50 years compared to the experiment using both elliptical tides and the critical velocity. Hence the differences in the critical velocity for sand erosion (related to the grain size) and the tidal ellipticity might explain the different wavelength of the ridges at those locations. The modeled orientation angles are around $-40°$ for all the experiments above, whilst the observed orientations are $-25°$ and $-6°$ for the Dutch Banks and the Flemish Banks, respectively.

It should be noted that the observed ridges have finite height. Nonlinear processes are likely to affect the wavelength of the bedforms during their long-term evolution. This behavior has been found in the case of other coastal bedforms, such as sand bars in the near shore zone (Garnier et al., 2006) and shoreface-connected sand ridges on the inner shelf (Nnafie et al., 2014).

Regarding long bed waves, Exp. 9 was designed to mimic the situation in the bottom boxed area of Fig. 1. Several long bed wave modes are found from the model results, the wavelength of these being in the range of 1.2–2.7 km. These values are similar to that of the observed long bed waves (1.6 km). The orientation angles are 11–33° and 60° for the modeled and observed cyclonically oriented bedforms, respectively, whilst for anticyclonically oriented long bed waves, the numbers are 16–22° and 30°, respectively. Thus, regarding the orientation, qualitative agreement is obtained for

long bed waves. The reason for the differences in the observed and modeled orientations is discussed in the next subsection.

4.5. Limitations

The present model is idealized in the sense that several assumptions have been made. First, the depth-averaged shallow water equations are used, which means that the vertical flow structure is not considered. Hence the model is not able to simulate sand waves (Hulscher, 1996; Besio et al., 2006; Borsje et al., 2013). The difference between modeled and observed orientation of tidal sand ridges and long bed waves could also be attributed to that assumption, since the direction of the currents near the bottom may differ from that of depth-averaged currents. Second, the domain size is assumed to be much smaller than the wavelength of tidal waves, so no phase differences of the background tidal waves are accounted for. Third, the model assumes a constant mean depth and periodic boundary conditions in all horizontal directions, thereby mimicking the situation on an open shelf, without considering the proximity of coasts. Fourth, the sand is uniform, so sorting processes (Walgreen et al., 2004; Roos et al., 2007) resulting in variation of mean grain size over the ridges are not accounted in the present model. Also note that although multiple tidal constituents in the forcing are considered, the residual flow and the nonlinear overtides of the principal tidal constituents are not included in this study. Finally, for simplicity, the orientations of tidal ellipses are chosen to be the same in the cases in which multiple tidal constituents are used.

4.6. Choice of numerical aspects

Regarding the choice of the bottom modes, the domain size (L_x, L_y) was chosen in the range of 1–36 km, and (k_x, k_y) were calculated from (L_x, L_y). In Exp. 1, 17×35 pairs of (k_x, k_y) were used. In the part of the (ϑ, k) parameter space where tidal sand ridges were expected ($-60° \leq \vartheta \leq -10°$ and $0 \leq k \leq 1.5$ rad/km), a minimum of 25×20 pairs of (ϑ, k) were used. For long bed waves, usually 57×25 pairs of (ϑ, k) were used.

Regarding the numerical settings, it has been demonstrated that using the grid size and time step mentioned in Subsection 2.5, the model results agree well with those of the previous studies. By using a smaller grid size $\Delta y = 100$ m and a time step $\Delta t = 5$ s instead of $\Delta y = 200$ m and $\Delta t = 10$ s for Exp. 1, it turned out that the relative change in the e-folding time of the fastest growing mode is 0.4%. Hence, the effect of the numerical discretization on the final results is very small. The initial amplitude of the bottom perturbation used in this study, i.e., $0.001H$, is adequate. Further experiments using amplitudes of $0.0001H$ and $0.01H$ of the bed perturbation for Exp. 1 revealed that the fastest growing mode has the same characteristics as that using $0.001H$.

5. Conclusions

Previous work has explained the mechanism of the generation of tidal sand ridges and long bed waves in coastal seas by free instability of the sandy bed subject to tidal currents. However, little attention has been paid to the effect of bed shear stress formulations (linear versus nonlinear), tidal characteristics (tidal ellipticity, different tidal constituents) and sand transport formulations on the characteristics (growth rate, wavelength, and orientation) of these large-scale bedforms during their initial formation. To this end, an idealized nonlinear numerical model was developed, which describes the interaction between depth-averaged tidal currents and the sandy bed. The results demonstrate that the present model is able to reproduce the initial formation of

tidal sand ridges and long bed waves as were found in earlier studies that employed linear stability analysis (Hulscher et al., 1993; Blondeaux et al., 2009). The advantage of the present approach is that it offers a framework to study the long-term nonlinear evolution of these bedforms, which will be done in future research.

For tidal sand ridges, using nonlinear bed shear stress and anisotropic slope-induced sand transport causes a slight increase of the growth rate and a decrease of the wavelength of the preferred bedforms. Furthermore, if the critical depth-averaged velocity for sand erosion is increased, the growth rate of the preferred bedforms becomes smaller, as well as the wavelength and the angle between the principal current direction and the crests. Note that besides tidal sand ridges, long bed waves could also emerge if the critical velocity is close to the maximum current velocity. The changes of the growth rate, wavelength and orientation angle of the preferred bedforms due to changing tidal ellipticity are non-monotonic: the largest growth rate and the smallest orientation angle are found around $\varepsilon = -0.2$, and the smallest wavelength is found around $\varepsilon = 0.2$. The combined effect of the critical velocity for sand erosion and elliptical tides might explain the difference in the wavelength at the Dutch Banks and the Flemish Banks in the North Sea. Using a diurnal tide increases the wavelength of the preferred bedforms significantly, while the orientation angle slightly decreases and the growth rate barely varies. The characteristics of the preferred bedforms are determined by the dominant tidal constituent if tidal currents with more than one constituents are considered. At locations dominant by the mixed tides, if the semidiurnal tide is known, as the amplitude of the diurnal tide increases, both the growth rate and the wavelength of the preferred bedforms increase. In the case of spring-neap tide dominant areas, if the representative current velocity is fixed, the growth rate hardly changes, while the bedforms with longer wavelength are found if the amplitudes of the two semidiurnal tides are close to each other. The change in the orientation of the preferred bedforms is insignificant for mixed tides and spring-neap tides.

Critical bed shear stress for sand erosion plays a key role in the generation of long bed waves: long bed waves appear if the critical velocity for sand erosion is slightly smaller than the maximum current velocity. In addition, in the Northern Hemisphere, if the tidal ellipticity is relatively large, more anticyclonically oriented long bed waves are observed for cyclonic tidal currents, while more cyclonically oriented long bed waves are found for anticyclonic tidal currents. Moreover, the growth rate of cyclonically oriented long bed waves increases as the tidal ellipticity increases under anticyclonic tidal currents. Linear/nonlinear and isotropic/anisotropic slope-induced sand transport are not essential for the formation of long bed waves.

References

Besio, G., Blondeaux, P., Vittori, G., 2006. On the formation of sand waves and sand banks. J. Fluid Mech. 557, 1–27.

Blondeaux, P., de Swart, H.E., Vittori, G., 2009. Long bed waves in tidal seas: an idealized model. J. Fluid Mech. 636, 485–495.

Borsje, B.W., Roos, P.C., Kranenburg, W.M., Hulscher, S.J.M.H., 2013. Modeling tidal sand wave formation in a numerical shallow water model: the role of turbulence formulation. Cont. Shelf Res. 60, 17–27.

Caballeria, M., Coco, G., Falques, A., Huntley, D.A., 2002. Self-organization mechanisms for the formation of nearshore crescentic and transverse sand bars. J. Fluid Mech. 465, 379–410.

Carbajal, N., Montaño, Y., 2001. Comparison between predicted and observed physical comparison between predicted and observed physical features of sandbanks. Estuar., Coast. Shelf Sci. 52, 425–443.

Davies, A.M., Furnes, G.K., 1980. Observed and computed M_2 tidal currents in the North Sea. J. Phys. Oceanogr. 10, 237–257.

Deigaard, R., Drønen, N., Fredsøe, J., Jensen, J.H., Jørgensen, M.P., 1999. A morphological stability analysis for a long straight barred coast. Coast. Eng. 36, 171–195.

Dyer, K.R., Huntley, D.A., 1999. The origin, classification and modelling of sand banks and ridges. Cont. Shelf Res. 19, 1285–1330.

Fredsøe, J., Deigaard, R., 1992. Mechanics of Coastal Sediment Transport. World Scientific.

Garnier, R., Calvete, D., Falques, A., Caballeria, M., 2006. Generation and nonlinear evolution of shore-oblique/transverse sand bars. J. Fluid Mech. 567, 327–360.

Hulscher, S.J.M.H., 1996. Tidal-induced large-scale regular bed form patterns in a three-dimensional shallow water model. J. Geophys. Res. 101 (C9), 20727–20744.

Hulscher, S.J.M.H., de Swart, H.E., de Vriend, H.J., 1993. The generation of offshore tidal sand banks and sand waves. Cont. Shelf Res. 13 (11), 1183–1204.

Huthnance, J.M., 1982. On one mechanism forming linear sand banks. Estuar. Coast. Shelf Sci. 14, 79–99.

Klein, M.D., Schuttelaars, H.M., 2005. Morphodynamic instabilities of planar beaches: sensitivity to parameter values and process formulations. J. Geophys. Res. 110 (F04S18). http://dx.doi.org/10.1029/2004JF000213.

Knaapen, M.A.F., Hulscher, S.J.M.H., de Vriend, H.J., 2001. A new type of sea bed waves. Geophys. Res. Lett. 28 (7), 1323–1326.

Liu, Z., Xia, D., Berne, S., Wang, K., Marsset, T., Tang, Y., Bourillet, J., 1998. Tidal deposition systems of China's continental shelf, with special reference to the eastern Bohai Sea. Mar. Geol. 145, 225–253.

McCave, I.N., 1979. Tidal currents at the North Hinder Lightship, southern north sea: flow directions and turbulence in relation to maintenance of sand banks. Mar. Geol. 31, 101–114.

Miller, M.C., McCave, I.N., Komar, P.D., 1977. Threshold of sediment motion under unidirectional currents. Sedimentology 24, 507–527.

Nnafie, A., de Swart, H.E., Calvete, D., Garnier, R., 2014. Modeling the response of shoreface-connected sand ridges to sand extraction on an inner shelf. Ocean Dyn. 64, 723–740.

Off, T., 1963. Rhythmic linear sand bodies caused by tidal currents. Bull. Am. Assoc. Pet. Geol. 47, 324–341.

Roos, P.C., Hulscher, S.J.M.H., de Vriend, H.J., 2008. Modelling the morphodynamic impact of offshore sandpit geometries. Coast. Eng. 55, 704–715.

Roos, P.C., Hulscher, S.J.M.H., Knaapen, M.A.F., 2004. The cross-sectional shape of tidal sandbanks: modelling and observation. J. Geophys. Res. 109, F02003.

Roos, P.C., Hulscher, S.J.M.H., Peters, B., Nemeth, A., 2001. A simple morphodynamic model for sand banks and large-scale sand pits subject to asymmetrical tides. In: Ikeda, S. (Ed.), Proceedings of the 2nd IAHR Symposium on River, Coastal and Estuarine Morphodynamics. IAHR, Hokkaido, Japan, pp. 91–100.

Roos, P.C., Wemmenhove, R., Hulscher, S.J.M.H., Hoeijmakers, H.W.M., Kruyt, N.P., 2007. Modeling the effect of nonuniform sediment on the dynamics of offshore tidal sandbanks. J. Geophys. Res. 112 (F02011). http://dx.doi.org/10.1029/2005JF000376.

Ryan, W.B.F., Carbotte, S.M., Coplan, J., O'Hara, S., Melkonian, A., Arko, R., Weissel, R., Ferrini, V., Goodwillie, A., Nitsche, F., Bonczkowski, J., Zemsky, R., 2009. Global multi-resolution topography synthesis. Geochem. Geophys. Geosyst. 10 (Q03014). http://dx.doi.org/10.1029/2008GC002332.

Sanders, J.A., Verhulst, F., Murdock, J., 2007. Averaging Methods in Nonlinear Dynamical Systems, 2nd edition. Springer Science & Business Media.

Seminara, G., 1998. Stability and morphodynamics. Meccanica 33, 59–99.

Talmon, A., Struiksma, N., Mierlo, M.V., 1995. Laboratory measurements of the direction of sediment transport on transverse alluvial-bed slopes. J. Hydraul. Res. 33 (4), 495–517.

van Dijk, T., van der Tak, C., de Boer, W., Kleuskens, M., Doornenbal, P., Noorlandt, R., Marges, V., 2011. The scientific validation of the hydrographic survey policy of the Netherlands Hydrographic Office, Royal Netherlands Navy. Tech. Rep. 1201907-000-BGS-0008, Deltares.

van Lancker, V.R., Bonne, W., Garel, E., Degrendele, K., Roche, M., den Eynde, D.V., Bellec, V., Brière, C., Collins, M.B., Velegrakis, A.F., 2010. Recommendations for the sustainable exploitation of tidal sandbanks. J. Coast. Res. 51, 151–164.

van Santen, R.B., de Swart, H.E., van Dijk, T.A.G.P., 2011. Sensitivity of tidal sand wavelength to environmental parameters: a combined data analysis and modelling approach. Cont. Shelf Res. 31, 966–978.

Walgreen, M., Calvete, D., de Swart, H.E., 2002. Growth of large-scale bed forms due to storm-driven and tidal growth of large-scale bed forms due to storm-driven and tidal currents: a model approach. Cont. Shelf Res. 22, 2777–2793.

Walgreen, M., de Swart, H.E., Calvete, D., 2004. A model for grain-size sorting over tidal sand ridges. Ocean Dyn. 54, 374–384.

Zimmerman, J.T.F., 1981. Dynamics, diffusion and geomorphological significance of tidal residual eddies. Nature 290 (5807), 549–555.

Zimmerman, J.T.F., 1982. On the Lorentz linearization of a quadratically damped forced oscillator. Phys. Lett. 89A (3), 123–124.